Journal of Biomedical Optics

SPIEDigitalLibrary.org/jbo

Quantitative photoacoustic imaging: correcting for heterogeneous light fluence distributions using diffuse optical tomography

Adam Q. Bauer
Ralph E. Nothdurft
Todd N. Erpelding
Lihong V. Wang
Joseph P. Culver

Quantitative photoacoustic imaging: correcting for heterogeneous light fluence distributions using diffuse optical tomography

Adam Q. Bauer,[a] Ralph E. Nothdurft,[a] Todd N. Erpelding,[b] Lihong V. Wang,[c] and Joseph P. Culver[a,c]
[a]Washington University School of Medicine, Department of Radiology, St. Louis, Missouri 63110
[b]Philips Research North America, 345 Scarborough Rd., Briarcliff Manor, New York 10510
[c]Washington University in Saint Louis, Department of Biomedical Engineering, St. Louis, Missouri 63130

Abstract. The specificity of molecular and functional photoacoustic (PA) images depends on the accuracy of the photoacoustic absorption spectroscopy. The PA signal is proportional to the product of the optical absorption coefficient and local light fluence; quantitative PA measurements of the optical absorption coefficient therefore require an accurate estimation of optical fluence. Light-modeling aided by diffuse optical tomography (DOT) can be used to map the required fluence and to reduce errors in traditional PA spectroscopic analysis. As a proof-of-concept, we designed a tissue-mimicking phantom to demonstrate how fluence-related artifacts in PA images can lead to misrepresentations of tissue properties. To correct for these inaccuracies, the internal fluence in the tissue phantom was estimated by using DOT to reconstruct spatial distributions of the absorption and reduced scattering coefficients of multiple targets within the phantom. The derived fluence map, which only consisted of low spatial frequency components, was used to correct PA images of the phantom. Once calibrated to a known absorber, this method reduced errors in estimated absorption coefficients from 33% to 6%. These results experimentally demonstrate that combining DOT with PA imaging can significantly reduce fluence-related errors in PA images, while producing quantitatively accurate, high-resolution images of the optical absorption coefficient. [DOI: 10.1117/1.3626212]

Keywords: quantitative photoacoustic imaging; diffuse optical tomography; light modeling; multimodal imaging.

Paper 11132 received Mar. 18, 2011; revised manuscript received Jul. 27, 2011; accepted for publication Jul. 29, 2011; published online Sep. 1, 2011.

1 Introduction

Photoacoustic imaging (PAI) is capable of providing high-resolution images of anatomy,[1] brain structure,[2] functional organization of the cerebral cortex,[2–4] and has been used to detect breast cancer in humans[5,6] and melanoma cells in rats.[3] With the advent of bioconjugated-, tunable-optical contrast agents (e.g., gold nanoparticles or carbon nanotubes), molecular PAI is also possible.[7–15] However, the ability to interpret molecular or functional contrast depends on the reliability of the PAI absorption spectroscopy.[16] If the absorption spectrum of the sample is known, then it would be possible, for example, to calculate the chromophore concentrations of interest. The relative photoacoustic (PA) signal is a product of both the optical absorption coefficient (the quantity of interest) and the local light fluence. Thus, spatial and spectral inhomogeneities in the fluence may undermine spectral interpretation of PA images. A noninvasive solution to this problem is to combine PAI with diffuse optical tomography (DOT).

Diffuse optical tomography is a clinically relevant imaging technology enabling researchers to study physiological processes (e.g., metabolism[17,18] and hemodynamics[17–20]), and is capable of reconstructing quantitative maps of optical properties,[18,21] albeit at lower resolution compared with PAI. DOT reconstructions of scattering and absorption can be used in conjunction with diffuse light modeling to generate the fluence information required to improve PA absorption spectroscopy. In this study, we demonstrate the use of a noninvasive hybrid imaging modality that combines PAI with DOT to circumvent sources of artifact in PAI. Although there has been some success in achieving quantitative information from PA images, previous studies have largely been done in simulation,[22–28] or applied iterative approaches using the PA image in conjunction with a light transport model to arrive at a least squares solution of the absorption coefficient by assuming uniform bulk optical properties.[24,29–32] With our hybrid technique, DOT is used to recover low-resolution absorption and reduced scattering coefficient maps of a tissue-mimicking phantom that was initially imaged in a PAI system. The optical properties and the nonuniform surface fluence pattern of the PAI system are input parameters to a light-tissue model that calculates the fluence throughout the phantom. This fluence distribution is then used to correct the PA image of the phantom, resulting in an accurate quantitative image of the absorption coefficient.

2 Materials and Methods

2.1 *Tissue-Mimicking Phantoms*

In order to evaluate sources of artifacts in PA images and the quantitative accuracy of our compensation algorithms, tissue-mimicking phantoms were designed with heterogeneous optical properties [Fig. 1(a)]. The agarose (Sigma-Aldrich, Saint

Address all correspondence to: Adam Quentin Bauer, Washington University School of Medicine, Radiology Department, East Building - 4525 Scott Avenue, Saint Louis, Missouri 63110. Tel: 314-362-6942; E-mail: abauer@hbar.wustl.edu.

1083-3668/2011/16(9)/096016/7/$25.00 © 2011 SPIE

Louis, Missouri), intralipid (20% fat emulsion, Fresenius Kabi, Germany), and India ink (Speedball, Statesville, North Carolina) reference mixture (absorption coefficient $\mu_a = 0.06\ \mathrm{cm}^{-1}$ at 780 nm and $0.07\ \mathrm{cm}^{-1}$ at 650 nm, and reduced scattering coefficient $\mu_s' = 5\ \mathrm{cm}^{-1}$ at 780 nm and $7.2\ \mathrm{cm}^{-1}$ at 650 nm) is poured into a mold and allowed to solidify at room temperature. Within this reference mixture, two types of inclusions were studied: 500 μm inner-diameter capillary tubes (BD Intramedic PE 50, Ontario, Canada) filled with 2% India ink ($\mu_a = 30\ \mathrm{cm}^{-1}$ at 780 nm, $36\ \mathrm{cm}^{-1}$ at 650 nm) placed at a depth of 12 mm, and larger (length $\times$ width $\times$height, 10 cm $\times$1 cm $\times$0.2 cm) rectangular scattering (4$\times$background) and absorption (5$\times$ background) perturbations placed 4 mm deep in the phantom, 8 mm above the tubes. The larger agarose inclusions were designed to aberrate the fluence profile while maintaining physiological values for absorption and scattering contrasts.

2.2 *Photoacoustic Imaging*

The PAI system used in this experiment [Fig. 1(b)] was modified from a clinical ultrasound (US) array system (iU22, Philips Healthcare, Andover, Massachusetts) and is described in a previous publication.[33] Briefly, the original channel board architecture of the US imaging system was modified to acquire raw, per-channel PA and US data. Raw radio-frequency data were transferred to a data acquisition computer where post-processing was performed. The data acquisition system controlled the laser firing and optical-wavelength tuning. PA images were processed using Fourier beam-forming reconstruction,[34] and displayed at $\sim$1 fps. The maximum data acquisition rate is 10 fps, limited by the current laser repetition rate. A linear 128-element US probe with a nominal bandwidth of 4 to 8 MHz (L8-4, Philips Healthcare) was physically integrated with a bifurcated optical fiber bundle (Light Guide Optics, Los Angeles, California), forming a hand-held probe. Laser pulses with a 6.5 ns pulse duration and 10 Hz repetition rate were generated from a tunable dye laser (Precision Scan-P, Sirah, Germany) tuned to 650 nm and pumped by a Q-switched Nd:yttrium–aluminum–garnet laser (Quanta-Ray Pro-350, Newport, Irvine, California). The US probe and incident fluence were coupled to the phantom via water bath. Twenty-one sites along the phantom were investigated in the orientation shown in Fig. 1(b) by translating the integrated US probe/fiber bundle in 3 mm increments along the targets. At each location, 100 frames were collected and averaged to improve signal-to-noise in the PA images. The US signals collected by the probe extend through 5 cm in depth, but the PA images reported have been cropped to a depth of 1.8 cm to only display relevant phantom information.

2.3 *Diffuse Optical Tomography*

The details of the experimental DOT system [Fig. 1(c)] can be found in a previous publication from our lab.[21] Briefly, a mode-locked Ti:Sapphire laser (pulse width $<$100 fs, pulse repetition rate = 80 MHz, MTS, Kapteyn-Murnane Labs, Boulder, Colorado) operating at 780 nm peak wavelength is pumped by a 6 W, 532 nm DPSS laser (Verdi, Coherent, Santa Clara, California) and illuminates the phantom in a transmission geometry. The beam is steered by an x-y galvanometer pair (AO, Model 6230, Cambridge Technology, Lexington, Mississippi) to illuminate the imaging chamber at 26 locations separated by 2 mm. An ultrafast image intensifier (PicoStarHR-12, LaVision, Inc., Ypsilanti, Michigan) relays time-gated images of the transmitted light levels on the detection plane to an EMCCD camera (iXon 877f, Andor Technologies, South Windsor, Connecticut). In this configuration, 48 time gates (400 ps wide, separated by 50 ps) sampled the transmitted light pulse at each of the 26 sites. Fourier transformation of the time-domain data provides frequency-domain information from 156 MHz to 1.6 GHz. For the reconstructions reported here, we used 313 MHz; this modulation frequency was found to provide an adequate balance of contrast between the absorption and scattering inclusions.[21]

Differential image reconstructions were obtained using a linear Rytov approximation approach. In this scheme the total

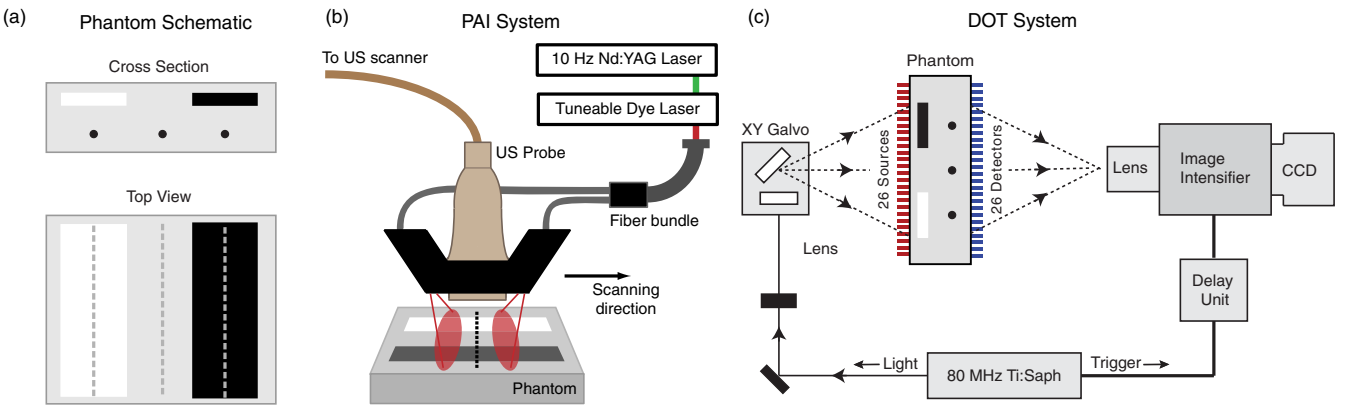

Fig. 1 Experimental layout. (a) Schematic of phantom showing the cross-sectional and overhead distribution of imbedded targets. Two large rectangular targets provide absorption and scattering contrast (5 times background and 4 times background, respectively) and produce inhomogeneous fluence profiles for the three identical deeper capillary tubes. (b) Subset of PAI system: fiber coupled light from a pumped dye laser irradiates the surface of the phantom in a dark-field illumination configuration. PA signals are acquired by a clinical ultrasound linear array. Twenty-one PA images were acquired by translating the probe in the direction shown; vertical dotted line under ultrasonic probe marks approximate location of PA image with respect to the probe. (c) Time-domain DOT system: a pulsed source beam is steered by a pair of galvanometer scanning mirrors to the source side of an imaging cassette. Light emitted from the detector plane is of the cassette is collected by a lens and temporally gated by an ultrafast gated image intensifier and detected by an EMCCD camera.

diffuse fluence, φ, is written

$$\varphi = \varphi_0 e^{\varphi_{scat}}. \quad (1)$$

The total fluence, φ, consists of a background field, φ_0, that depends on background optical properties, and a perturbed field, φ_{scat}, that is linearly related to a set of spatial variations in the optical properties: absorption, μ_a, and the diffusion coefficient, D, where $D = v/3\mu_s'$, μ_s' is the reduced scattering coefficient, and v is the speed of light in the medium. Experimental measurements of φ on the sample surface lead to images of spatially varying absorption and reduced scattering coefficients via solution of a least squares problem. The reconstruction procedures are outlined by Patwardhan et al.[21]

2.4 *Hybrid DOT-PAI*

A photoacoustic image directly reports the acoustic pressure distribution, $p_0(x, \lambda)$, arising from localized optical absorption. The absorbed optical energy density, $h(x, \lambda)$, and $p_0(x, \lambda)$, are related by

$$p_0(x, \lambda) = \Gamma(x) h(x, \lambda), \quad (2)$$

where the Grueisen parameter, $\Gamma(x)$ is a thermodynamic property of the tissue.[35] The absorbed optical energy density, $h(x, \lambda)$, is equal to the optical fluence distribution, $\varphi(x, \lambda)$, multiplied by the optical absorption coefficient, $\mu_a(x, \lambda)$, within the irradiated medium, i.e.,

$$h(x, \lambda) = \varphi(x, \lambda)\mu_a(x, \lambda). \quad (3)$$

PAI directly reconstructs the pressure field, $p_0(x, \lambda)$, which is proportional to both the optical absorption coefficient and optical fluence distribution within the irradiated medium. Rearranged, Eq. (3) can be expressed as a formula for the absorption coefficient,

$$\mu_a(x, \lambda) = \frac{1}{\Gamma(x)} \frac{p_0(x, \lambda)}{\varphi(x, \lambda)}. \quad (4)$$

In this study, the continuous wave fluence in the phantom was calculated by solving the diffuse photon density wave equation,

$$\nabla \cdot [D(r)\nabla\varphi(r)] - v\mu_a(r)\varphi(r) = -vS(r), \quad (5)$$

using a finite difference method.[36] Inputs into the calculation were the spatially-varying absorption and scattering maps of the DOT reconstructions, and the surface illumination pattern of the PAI system for the source term, $S(r)$. Because the DOT and PAI systems operate at different wavelengths, the absorption and scattering coefficients were spectrally mapped from 780 to 650 nm. The absorption properties of the India ink were fully characterized from 400 to 900 nm with a spectrophotometer (DU640, Beckman Coulter, Inc., Brea, California), and μ_a of the India ink was measured to be 0.07 cm^{-1} at 650 nm, while μ_s' of the intralipid was calculated to be 7.2 cm^{-1} at 650 nm using Mie theory.[37] The scattering inclusion in the phantom was mixed to have a reduced scattering coefficient 4 times that of the background, and the large absorption inclusion and was designed to be 5 times the background absorption. After reconstructing the optical property maps at 780 nm with the DOT system, the absorption image was scaled by the ratio of the absorption coefficient at 650 and 780 nm, and the reduced scattering images was scaled by the ratio of the reduced scattering coefficient at 650 and 780 nm. Although it is unfortunate that the time-domain DOT system did not operate over the same wavelength range as the PAI system, this difference in wavelength should not pose a significant problem to the methodology as both intralipid and India ink are well characterized and relatively spectrally flat[37,38] (i.e., the absorption and scattering properties monotonically decrease with increasing wavelength, with no peaks or troughs over the spectral region investigated).

3 Results

The PAI system reconstructs a cross-sectional image (depth versus azimuth) of the phantom at the dashed line between the two elliptical illumination patterns of the fiber bundles in Fig. 1(b). The PA reconstruction [Fig. 2(a)] shows with high resolution all three capillary tubes and the large absorbing target. However, PAI cannot reconstruct scattering perturbations. PA signals are not generated from optical scatterers so the rectangular scattering target does not provide any source of photoacoustic contrast in the PA image. Two artifacts of PAI can also be seen in Fig. 2(a): 1. Pressure fields generated outside the effective bandwidth of the transducer are not detected. This results in the

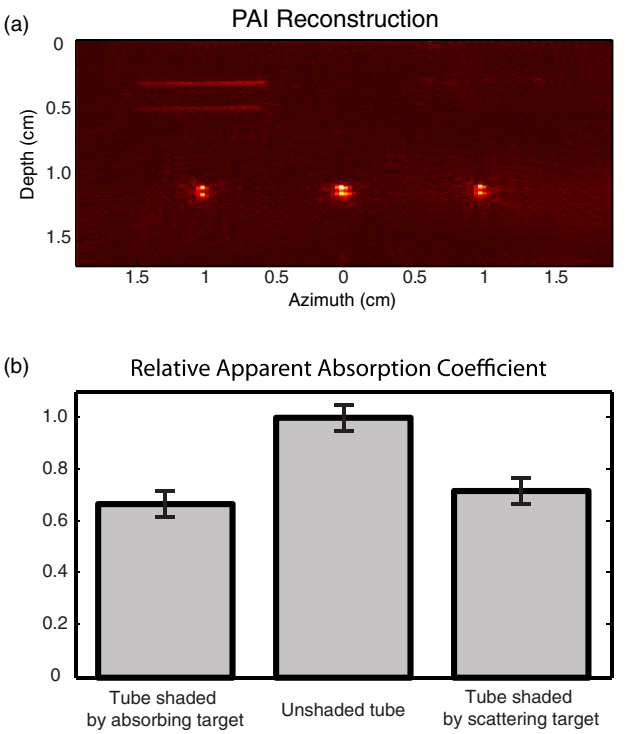

Fig. 2 Raw photoacoustic reconstruction. (a) PA image showing a cross-section of the phantom. Note the complete absence of the scattering target in addition to the different signal magnitudes of the three 1.2-mm deep, optically-identical capillary tubes. (b) Volume-integrated PA signal magnitude of the three capillary tubes, normalized to the middle tube. Due to the inhomogeneous fluence distribution within the bulk of the phantom, the three capillary tubes produce PA signals of different magnitudes. The mean PA signal of the two outer, shaded tubes differs in magnitude with the unshaded middle tube by ~33%. Errors bars represent the standard deviation of the mean PA signal magnitude of each tube measured at the 21 sites (standard deviation for each tube is between 7% and 8% of the mean).

spatial-derivative–like appearance of the objects detected by this system (most notably the larger rectangular absorber near the surface). The top and bottom surfaces of the large absorbing target and the smaller capillary tubes are the only portions that produce US frequency components within the nominal 4 to 8 MHz bandwidth of the US probe. And, 2. the PA signal from the three optically-identical capillary tubes are significantly different in magnitude, presumably due to the uneven fluence profile created by the presence of the two shallower absorbing and scattering targets above, as well as the incident shape of the surface fluence pattern. Artifact 2. is characterized in Fig. 2(b) where the signals from each target are volume integrated (FWHM, with an equal number of pixels included in the integral) and normalized to the middle tube. Over the 21 sites investigated, the mean PA signals from the two shaded outer targets are as much as 33% less than the mean PA signal of the middle target. In addition, the PA signal emerging from the bottom surface of the rectangular absorber [∼5 mm deep in Fig. 2(a)] is less than the signal from the top surface (∼3 mm deep). Even over this 2 mm length scale, fluence-related artifacts are apparent in a single target. By combining PAI with DOT, one can recover scattering contrasts (to which PAI is not sensitive) and address the fluence-related Artifact 2. Artifact 1., while not addressed in this study, can be reduced through wide-band ultrasound detection schemes.[39–41]

DOT reconstructions of the absorption and scattering targets [Fig. 3(a)] depict very little crosstalk between the two contrasts. Although the resolution of the DOT reconstructions is markedly poorer than the PA image, the volume-integrated signals from the objects are quantitative with respect to background property values.[18,21] The surface fluence distribution of the PAI system [Fig. 3(b)] was obtained by photographing from below a piece of white paper placed the same distance from the transducer as the surface of the phantom imaged with this system. The lobed pattern of the source field in the PAI system is designed to minimize surface PA signals from saturating the US probe (situated between the two lobes, not shown). This technique is effective at generating better images near the surface, but this pattern will also produce inhomogeneous fluence throughout the imaging domain.

The calculated fluence [Fig. 3(c)] within the phantom using the optical property maps from the DOT reconstructions at the location of the PA image in Fig. 2(a) clearly illustrates the inhomogeneities caused by the inclusions and the surface illumination pattern. It can be seen from a normalized line profile of the fluence at the depth of the capillary tubes [Fig. 3(d)], that the reduction of the fluence at the location of the two shaded outer targets (located at -1 and 1 cm azimuthally) is approximately the same magnitude as the percent difference in the PA signals between the outer shaded tubes and the middle unshaded tube [Fig. 2(b)].

The fluence-related artifacts present in the original PA image can be corrected by dividing the raw PA image in Fig. 2(a) by the fluence image in Fig. 3(c) pixel-by-pixel. From this corrected image [Fig. 4(a)], the capillary tubes are all of equal brightness. It can also be seen that the top and bottom surfaces of the larger, shallower absorber are also of comparable brightness, though the overall brightness of this object is reduced from the original image because it is markedly lower in absorption compared with the capillary tubes. The fluence-compensated results are compared to the initial images using the volume-integrated signals over each capillary tube [Fig. 4(b)]. The average error between the outer shaded tubes is now within approximately 6% of the middle unshaded tube, i.e., the error in the original PA image has been reduced by ∼6 times.

4 Discussion

Absorption spectroscopy is a powerful aspect of photoacoustic imaging, yet it is highly susceptible to fluence heterogeneity. In a small animal imaging scenario, it is not uncommon to have orders-of-magnitude changes in light levels as one irradiates different sections of the animal.[21] In this study, where the fluence varies over an order of magnitude within the phantom, we have shown that a reduction in the light level by only a third can produce appreciable misrepresentations of observed optical absorption. Because estimations of the absorption coefficient are linearly related to chromophore concentration, in this scenario, the concentrations would be underestimated by 33%. Photoacoustic imaging without fluence correction is susceptible to artifacts caused by 1. structure in the illumination pattern, 2. attenuation of the light fluence due to bulk optical properties and determined by the tissue geometry, and 3. internal

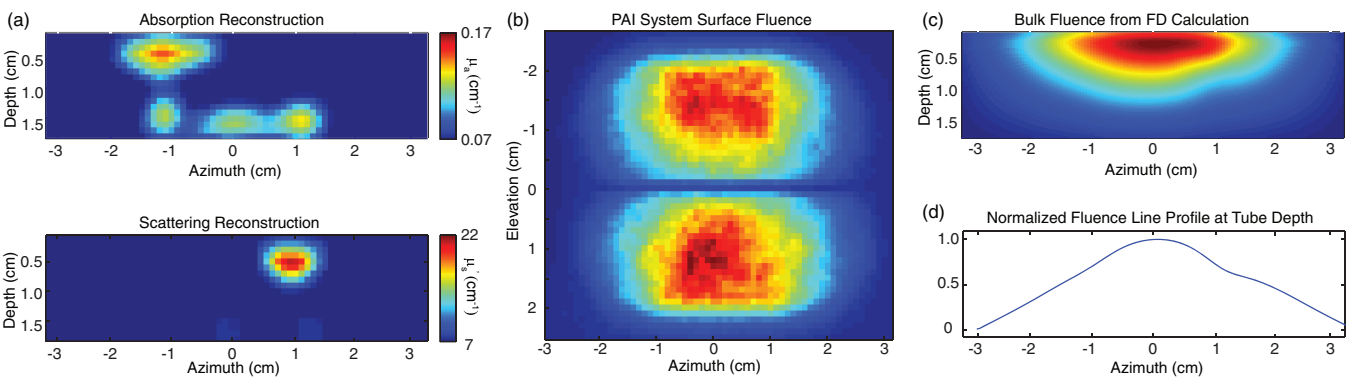

Fig. 3 DOT reconstruction data and fluence calculations. (a) DOT reconstructions of the absorption and scattering properties of the phantom. (b) Fluence pattern on the surface of the phantom during PA data collection. This source distribution and DOT reconstructions are used as the input to the finite difference solution of Eq. (5). (c) Cross-sectional slice of the bulk fluence distribution calculated using finite difference. (d) Fluence line profile at the depth of the capillary tubes (1.2 cm) showing azimuthal inhomogeneity. Note the reduction in fluence magnitude of approximately 33% at the location of the capillary tubes (± 1 cm azimuth)

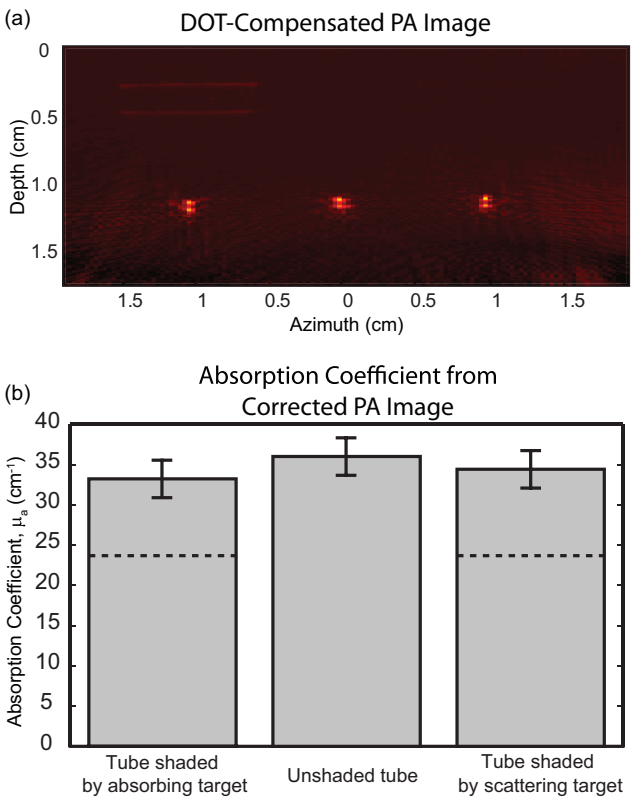

Fig. 4 PA data from Fig. 2 compensated by the DOT and surface fluence data shown in Fig. 3 using Eq. (4). (a) After DOT-assisted fluence correction, the three capillary tubes are all approximately of equal magnitude, and the top and bottom surfaces of the larger agarose inclusion are also of equal magnitude. (b) Volume-integrated absorption coefficient of the three capillary tubes. The discrepancy in the absorption coefficient in Fig. 2 can be reduced to 6% between the tubes with this method. Horizontal dotted lines indicate what would be estimated as the magnitude of the absorption coefficient of the outer tubes from original uncompensated PA image of Fig. 2(a). Errors bars represent the standard deviation of the mean PA signal magnitude of each tube measured at the 21 sites (standard deviation for each tube is between 7% and 8% of the mean).

absorption and scattering heterogeneities. For accurate spectral PAI, these factors need to be addressed and appropriately corrected. This study demonstrates the feasibility of correcting PAI for all three types of fluence inhomogenities using experimental data from a time-resolved DOT system and diffuse light modeling.

Previous experimental efforts to quantify photoacoustic images with diffusing-light measurements[30] used the measured light intensity along the surface of a phantom as a constraint on an iterative solution to a fluence calculation; however, homogeneous absorption and scattering were assumed in estimating the distribution of optical fluence in the phantom studied. In addition, the absorption perturbations imaged with the PA system were relatively small, low-contrast targets that minimally affected the bulk fluence. Although it does not apply to iterative methods in general, some experimental investigations toward quantifying PA images using this technique to converge on optical property data have shown that too many iterations can produce deleterious effects,[32] while more novel and robust quantification methods using sparse signal representation of PA signals[42] may still be beset by nonuniform surface illumination. The advantage of our method is that it properly accounts for both scattering and absorption targets and collectively solves for all three types of fluence inhomogeneities.

The compensation performed in this study assumed that the Gruneisen parameter, Γ, in Eqs. (2) and (4) to be constant and part of the calibration. This assumption is not unreasonable in this particular study as the targets in the phantom are all made of the same material or materials having very similar mechanical and thermodynamic properties. However, applying this methodology to another medium (e.g., mouse brain) may require a different calibration factor, and provided the tissues types are not drastically different (such as the mechanical and thermodynamic properties of fat and blood[35,43]), the assumption that Γ remains approximately constant may still be valid.

Ideally, the images acquired from the DOT and PAI systems should be obtained using the same wavelength. This restriction was relaxed here because the spectral characteristics of the absorption and scattering contrasts (India ink and intralipid) are slowly varying over a 400 to 900 nm range so that the optical properties at the PAI wavelength could be predicted from the DOT data at a different wavelength.[37,38] The DOT and PAI data sets were matched by mapping the optical properties acquired with the DOT system to those of the PAI system using the Mie theory for the intralipid, and quantitative broadband experimental spectroscopy for the India ink. Using the data from the spectrophotometer at 650 nm, this PAI system can be calibrated to the middle unshaded tube (which presumably represents the true absorption properties of all three tubes) to provide quantitative images of optical absorption. In moving this method forward to an *in vivo* setting, where the contrasts are more spectrally rich, it will be preferable to match the wavelengths of the DOT and PAI systems.

With DOT being used to compensate for PAI illumination, one strategy might be to have the DOT system use the same illumination structure as PAI. However, here, that is not the case. In either the DOT or PAI system, the type of illumination is chosen to maximize the sensitivity of the modality, with the structure of the interrogating light being best suited for the method used. Uniform, planar illumination is desired for many PAI applications, while discrete optodes are ideal for DOT measurements. For the compensation method presented here to work, it is not required that the DOT source pattern (discrete point sources) and the PAI source pattern (a lobed, dark-field surface pattern) have the same source illumination pattern. Provided the objects in the phantom have been sufficiently sampled by the DOT source grid, the optical property maps recovered from DOT measurements should be nearly unaffected by the density of measurements.[44,45] The illumination pattern of the PAI system is taken into account during the final diffuse light modeling of the fluence throughout the PA imaging domain.

The typical resolving capability of a DOT system, and therefore the resolution limit of the fluence estimate using DOT, is approximately 2 to 3 mm. However, the distribution of light fluence is, in general, comprised of low spatial frequency components—even high spatial frequency changes in μ_a (e.g., the transition from the bulk of the phantom to the rectangular absorbing target or capillary tubes) will not be observed in analysis of fluence profiles. Although the imaging resolution of DOT is relatively poorer than PA imaging, an advantage of using DOT to

estimate fluence profiles is that targets falling below the imaging resolution of the DOT system are still recovered, i.e., the optical property maps become volume-averaged quantities (e.g., cortical activations occurring on the capillary bed), which can still be used to accurately estimate light fluence. In a PA imaging system, objects falling below the imaging resolution of the US transducer (which depends on the bandwidth and center frequency of the probe) are not seen at all—as in the case of the bulk of the larger rectangular targets in the phantom, and the bulk of the phantom itself. In the case of a spatially-rapid absorption change (e.g., a thrombus within a vessel during an ischemic event) the rapid change in blood flow at the occlusion will be spread over a relatively larger area in the DOT image, and more localized in a PA image. In this instance, a higher-resolution PAM image of smaller vessels ($\sim$10 μm), or a lower-resolution PAT image of larger vessels (hundreds of micrometers to millimeters) would each provide complementary data sets to the DOT image.

Here we have demonstrated a method to correct PA images for fluence heterogeneities at a depth significantly deeper than 1 mm using diffuse optical tomography where each pixel in the 2-D source pattern from the PA imaging system is modeled as an exponentially-decaying collimated source within the diffusion approximation.[36] This method has been shown to represent more accurately the remitted flux of photons on the object's surface, as well as the flux of photons propagating forward in the object.[46,47] Because photoacoustic microscopy operates at distances near to and shallower than 1mm, in this situation, in may be beneficial to utilize light modeling methods based on the more accurate radiative transport equation (e.g., using Monte Carlo techniques). Although PA signals will always depend on the fluence profile of the illumination, PA signals originating from objects within tens to hundreds of microns of the surface may not be subject to the other "shading" types of fluence related artifacts also addressed in this study.

For some clinical applications, it will likely be necessary to also have the DOT data set acquired with reflection-mode instrumentation. For example, in human neuroimaging, fluence distributions over many orders of magnitude have been detected and modeled with sufficient signal-to-noise to be capable of reconstructing endogenous chromophore concentrations in the adult[48,49] and infant brain,[50] as well as in brain-mimicking phantoms.[51,52] So, in principle, compensating PA images with DOT measurements should work equally well in an imaging scenario involving larger variations in light fluence. While the relative error in the data presented here was reduced by a factor of $\sim$6 (33% to 6%), the remaining uncertainty in the optical absorption coefficient of the capillary tubes is most likely due to inhomogeneities in the optical properties of the ingredients in the phantom (the India Ink is a suspension of carbon powder, which is prone to aggregation), the lateral sensitivity of the US probe, and aberrations in the detected pressure field causing phase cancellation artifacts at the US receiver surface.[53]

5 Conclusions

We have shown that quantitative PAI is possible when coupled with DOT. Traditional PAI may contain fluence-related errors which can render photoacoustic spectroscopy both quantitatively and qualitatively inaccurate. To compensate for PA images acquired in this study, low resolution DOT reconstructions of a phantom's optical properties were used in conjunction with the surface fluence profile of the PAI system to numerically calculate the fluence throughout the phantom. This fluence distribution was then used to correct PA images, yielding quantitative information about targets 1.2-cm deep in the phantom. Before compensation, three optically-identical PA targets were found to differ in PA signal magnitude by 33%. This considerable error was reduced to 6% with the methods described herein. These results motivate development of an integrated PAI-DOT system for concurrent *in vivo* imaging.

Acknowledgments

This work was supported in part by NIH Grant Nos. R01-EB008085 and U54 CA136398.

References

1. K. Maslov, H. F. Zhang, S. Hu, and L. V. Wang, "Optical-resolution photoacoustic microscopy for in vivo imaging of single capillaries," *Opt. Lett.* **33**(9), 929–931 (2008).
2. X. D. Wang, Y. J. Pang, G. Ku, X. Y. Xie, G. Stoica, and L. H. V. Wang, "Noninvasive laser-induced photoacoustic tomography for structural and functional in vivo imaging of the brain," *Nat. Biotechnol.* **21**(7), 803–806 (2003).
3. H. F. Zhang, K. Maslov, G. Stoica, and L. H. V. Wang, "Functional photoacoustic microscopy for high-resolution and noninvasive in vivo imaging," *Nat. Biotechnol.* **24**(7), 848–851 (2006).
4. L. D. Liao, M. L. Li, H. Y. Lai, Y. Y. I. Shih, Y. C. Lo, S. N. Tsang, P. C. P. Chao, C. T. Lin, F. S. Jaw, and Y. Y. Chen, "Imaging brain hemodynamic changes during rat forepaw electrical stimulation using functional photoacoustic microscopy," *Neuroimage* **52**(2), 562–570 (2010).
5. A. A. Oraevsky, A. A. Karabutov, S. V. Solomatin, E. V. Savateeva, V. A. Andreev, Z. Gatalica, H. Singh, and R. D. Fleming, "Laser optoacoustic imaging of breast cancer in vivo," *Proc. SPIE* **4256**, 6–15 (2001).
6. S. Manohar, S. E. Vaartjes, J. C. van Hespen, J. M. Klaase, F. M. van den Engh, W. Steenbergen, and T. G. van Leeuwen, "Initial results of in vivo non-invasive cancer imaging in the human breast using near-infrared photoacoustics," *Opt. Express* **15**(19), 12277–12285 (2007).
7. J. W. Kim, E. I. Galanzha, E. V. Shashkov, H. M. Moon, and V. P. Zharov, "Golden carbon nanotubes as multimodal photoacoustic and photothermal high-contrast molecular agents," *Nat. Nanotechnol.* **4**(10), 688–694 (2009).
8. D. P. Pan, M. Pramanik, A. Senpan, X. M. Yang, K. H. Song, M. J. Scott, H. Y. Zhang, P. J. Gaffney, S. A. Wickline, L. V. Wang, and G. M. Lanza, "Molecular photoacoustic tomography with colloidal nanobeacons," *Angew. Chem., Int. Ed.* **48**(23), 4170–4173 (2009).
9. A. De La Zerda, C. Zavaleta, S. Keren, S. Vaithilingam, S. Bodapati, Z. Liu, J. Levi, B. R. Smith, T. J. Ma, O. Oralkan, Z. Cheng, X. Y. Chen, H. J. Dai, B. T. Khuri-Yakub, and S. S. Gambhir, "Carbon nanotubes as photoacoustic molecular imaging agents in living mice," *Nat. Nanotechnol.* **3**(9), 557–562 (2008)
10. A. Portnov, Y. Ganot, S. Rosenwaks, and I. Bar, "Probing molecular dynamics using action, Doppler and photoacoustic spectroscopy," *J. Mol. Struct.* **744**, 107–115 (2005).
11. C. Kim, E. C. Cho, J. Y. Chen, K. H. Song, L. Au, C. Favazza, Q. A. Zhang, C. M. Cobley, F. Gao, Y. N. Xia, and L. H. V. Wang, "In vivo molecular photoacoustic tomography of melanomas targeted by bioconjugated gold nanocages," *ACS Nano* **4**(8), 4559–4564 (2010).
12. L. Z. Xiang, Y. Yuan, D. Xing, Z. M. Ou, S. H. Yang, and F. F. Zhou, "Photoacoustic molecular imaging with antibody-functionalized single-walled carbon nanotubes for early diagnosis of tumor," *J. Biomed. Opt.* **14**(2), 021008 (2009).
13. P. C. Li, C. R. C. Wang, D. B. Shieh, C. W. Wei, C. K. Liao, C. Poe, S. Jhan, A. A. Ding, and Y. N. Wu, "In vivo photoacoustic molecular imaging with simultaneous multiple selective targeting using antibody-conjugated gold nanorods," *Opt. Express* **16**(23), 18605–18615 (2008).

14. V. Ntziachristos and D. Razansky, "Molecular imaging by means of multispectral optoacoustic yomography (MSOT)," *Chem. Rev.* **110**(5), 2783–2794 (2010).
15. J. A. Copland, M. Eghtedari, V. L. Popov, N. Kotov, N. Mamedova, M. Motamedi, and A. A. Oraevsky, "Bioconjugated gold nanoparticles as a molecular based contrast agent: Implications for imaging of deep tumors using optoacoustic tomography," *Mol. Imaging Biol.* **6**(5), 341–349 (2004).
16. J. Laufer, C. Elwell, D. Delpy, and P. Beard, "In vitro measurements of absolute blood oxygen saturation using pulsed near-infrared photoacoustic spectroscopy: accuracy and resolution," *Phys. Med. Biol.* **50**(18), 4409–4428 (2005).
17. J. P. Culver, T. Durduran, T. Furuya, C. Cheung, J. H. Greenberg, and A. G. Yodh, "Diffuse optical tomography of cerebral blood flow, oxygenation, and metabolism in rat during focal ischemia," *J. Cereb. Blood Flow Metab.* **23**(8), 911–924 (2003).
18. J. P. Culver, A. M. Siegel, J. J. Stott, and D. A. Boas, "Volumetric diffuse optical tomography of brain activity," *Opt. Letters* **28**(21), 2061–2063 (2003).
19. T. O. McBride, B. W. Pogue, E. D. Gerety, S. B. Poplack, U. L. Osterberg, and K. D. Paulsen, "Spectroscopic diffuse optical tomography for the quantitative assessment of hemoglobin concentration and oxygen saturation in breast tissue," *Appl. Opt.* **38**(25), 5480–5490 (1999).
20. C. Zhou, G. Q. Yu, D. Furuya, J. H. Greenberg, A. G. Yodh, and T. Durduran, "Diffuse optical correlation tomography of cerebral blood flow during cortical spreading depression in rat brain," *Opt. Express* **14**(3), 1125–1144 (2006).
21. S. V. Patwardhan and J. P. Culver, "Quantitative diffuse optical tomography for small animals using an ultrafast gated image intensifier," *J. Biomed. Opt.* **13**(1), 011009 (2008).
22. B. Banerjee, S. Bagchi, R. M. Vasu, and D. Roy, "Quantitative photoacoustic tomography from boundary pressure measurements: noniterative recovery of optical absorption coefficient from the reconstructed absorbed energy map," *J. Opt. Soc. Am. A* **25**(9), 2347–2356 (2008).
23. J. Ripoll and V. Ntziachristos, "Quantitative point source photoacoustic inversion formulas for scattering and absorbing media," *Phys. Rev. E* **71**(3), 031912 (2005).
24. B. T. Cox, S. R. Arridge, K. P. Kostli, and P. C. Beard, "Two-dimensional quantitative photoacoustic image reconstruction of absorption distributions in scattering media by use of a simple iterative method," *Appl. Opt.* **45**(8), 1866–1875 (2006).
25. B. T. Cox, S. R. Arridge, and P. C. Beard, "Estimating chromophore distributions from multiwavelength photoacoustic images," *J. Opt. Soc. Am. A* **26**(2), 443–455 (2009).
26. Z. Yuan and H. B. Jiang, "Simultaneous recovery of tissue physiological and acoustic properties and the criteria for wavelength selection in multispectral photoacoustic tomography," *Opt. Lett.* **34**(11), 1714–1716 (2009).
27. R. J. Zemp, "Quantitative photoacoustic tomography with multiple optical sources," *Appl. Opt.* **49**(18), 3566–3572 (2010).
28. G. Bal and G. Uhlmann, "Inverse diffusion theory of photoacoustics," *Inverse Probl.* **26**(8), (2010).
29. L. Yao, Y. Sun, and H. B. Jiang, "Quantitative photoacoustic tomography based on the radiative transfer equation," *Opt. Lett.* **34**(12), 1765–1767 (2009).
30. L. Yin, Q. Wang, Q. Z. Zhang, and H. B. Jiang, "Tomographic imaging of absolute optical absorption coefficient in turbid media using combined photoacoustic and diffusing light measurements," *Opt. Lett.* **32**(17), 2556–2558 (2007).
31. Z. Yuan and H. B. Jiang, "Quantitative photoacoustic tomography: Recovery of optical absorption coefficient maps of heterogeneous media," *Appl. Phys. Lett.* **88**(23), 231101 (2006).
32. T. Jetzfellner, D. Razansky, A. Rosenthal, R. Schulz, K. H. Englmeier, and V. Ntziachristos, "Performance of iterative optoacoustic tomography with experimental data," *Appl. Phys. Lett.* **95**(1), 019703 (2009).
33. T. N. Erpelding, C. Kim, M. Pramanik, L. Jankovic, K. Maslov, Z. J. Guo, J. A. Margenthaler, M. D. Pashley, and L. H. V. Wang, "Sentinel lymph nodes in the rat: noninvasive photoacoustic and US imaging with a clinical US system," *Radiology* **256**(1), 102–110 (2010).
34. K. P. Kostli, M. Frenz, H. Bebie, and H. P. Weber, "Temporal backward projection of optoacoustic pressure transients using Fourier transform methods," *Phys. Med. Biol.* **46**(7), 1863–1872 (2001).
35. F. Duck, *Physical Properties of Tissue: A Comprehensive Reference Book*, Academic Press, London (1990).
36. M. J. Holboke, B. J. Tromberg, X. Li, N. Shah, J. Fishkin, D. Kidney, J. Butler, B. Chance, and A. G. Yodh, "Three-dimensional diffuse optical mammography with ultrasound localization in a human subject," *J. Biomed. Opt.* **5**(2), 237–247 (2000).
37. R. Michels, F. Foschum, and A. Kienle, "Optical properties of fat emulsions," *Opt. Express* **16**(8), 5907–5925 (2008).
38. M. Canpolat and J. R. Mourant, "Monitoring photosensitizer concentration by use of a fiber-optic probe with a small source-detector separation," *Appl. Opt.* **39**(34), 6508–6514 (2000).
39. A. A. Karabutov, E. V. Savateeva, N. B. Podymova, and A. A. Oraevsky, "Backward mode detection of laser-induced wide-band ultrasonic transients with optoacoustic transducer," *J. Appl. Phys.* **87**(4), 2003–2014 (2000).
40. E. Zhang, J. Laufer, and P. Beard, "Backward-mode multiwavelength photoacoustic scanner using a planar Fabry-Perot polymer film ultrasound sensor for high-resolution three-dimensional imaging of biological tissues," *Appl. Opt.* **47**(4), 561–577 (2008).
41. S. L. Chen, S. W. Huang, T. Ling, S. Ashkenazi, and L. J. Guo, "Polymer microring resonators for high-sensitivity and wideband photoacoustic imaging," *IEEE Trans. Ultrason. Ferroelectr. Freq. Control* **56**(11), 2482–2491 (2009).
42. A. Rosenthal, D. Razansky, and V. Ntziachristos, "Quantitative optoacoustic signal extraction using sparse signal representation," *IEEE Trans. Med. Imag.* **28**(12), 1997–2006 (2009).
43. M. Toubal, M. Asmani, E. Radziszewski, and B. Nongaillard, "Acoustic measurement of compressibility and thermal expansion coefficient of erythrocytes," *Phys. Med. Biol.* **44**(5), 1277–1287 (1999).
44. E. E. Graves, J. P. Culver, J. Ripoll, R. Weissleder, and V. Ntziachristos, "Singular-value analysis and optimization of experimental parameters in fluorescence molecular tomography," *J. Opt. Soc. Am. A* **21**(2), 231–241 (2004).
45. J. P. Culver, V. Ntziachristos, M. J. Holboke, and A. G. Yodh, "Optimization of optode arrangements for diffuse optical tomography: A singular-value analysis," *Opt. Letters* **26**(10), 701–703 (2001).
46. D. Boas, J. Culver, J. Stott, and A. Dunn, "Three dimensional Monte Carlo code for photon migration through complex heterogeneous media including the adult human head," *Opt. Express* **10**(3), 159–170 (2002).
47. R. C. Haskell, L. O. Svaasand, T. T. Tsay, T. C. Feng, M. S. McAdams, and B. J. Tromberg, "Boundary conditions for the diffusion equation in radiative transfer," *J. Opt. Soc. Am. A Opt. Image. Sci. Vis.* **11**(10), 2727–2741 (1994).
48. D. A. Boas, K. Chen, D. Grebert, and M. A. Franceschini, "Improving the diffuse optical imaging spatial resolution of the cerebral hemodynamic response to brain activation in humans," *Opt. Lett.* **29**(13), 1506–1508 (2004).
49. B. W. Zeff, B. R. White, H. Dehghani, B. L. Schlaggar, and J. P. Culver, "Retinotopic mapping of adult human visual cortex with high-density diffuse optical tomography," *Proc. Natl. Acad. Sci. U. S. A.* **104**(29), 12169–12174 (2007).
50. S. M. Liao, N. M. Gregg, B. R. White, B. W. Zeff, K. A. Bjerkaas, T. E. Inder, and J. P. Culver, "Neonatal hemodynamic response to visual cortex activity: high-density near-infrared spectroscopy study," *J. Biomed. Opt.* **15**(2), 026010 (2010).
51. H. Dehghani, B. R. White, B. W. Zeff, A. Tizzard, and J. P. Culver, "Depth sensitivity and image reconstruction analysis of dense imaging arrays for mapping brain function with diffuse optical tomography," *Appl. Opt.* **48**(10), D137–143 (2009).
52. B. W. Pogue, K. D. Paulsen, C. Abele, and H. Kaufman, "Calibration of near-infrared frequency-domain tissue spectroscopy for absolute absorption coefficient quantitation in neonatal head-simulating phantoms," *J. Biomed. Opt.* **5**(2), 185–193 (2000).
53. A. Q. Bauer, K. R. Marutyan, M. R. Holland, and J. G. Miller, "Negative dispersion in bone: the role of interference in measurements of the apparent phase velocity of two temporally overlapping signals," *J. Acoust. Soc. Am.* **123**(4), 2407–2414 (2008).